Insights into the thermolytic transformation of lignocellulosic biomass waste to redox-active carbocatalyst: Durability of surface active sites

Wen-Da Oh[a,b,*], Grzegorz Lisak[b,c], Richard D. Webster[d], Yen-Nan Liang[b], Andrei Veksha[b], Apostolos Giannis[b], James Guo Sheng Moo[b], Jun-Wei Lim[e], Teik-Thye Lim[b,c,**]

[a] School of Chemical Sciences, Universiti Sains Malaysia, 11800 Penang, Malaysia
[b] Nanyang Environment and Water Research Institute (NEWRI), Nanyang Technological University, 1 Cleantech Loop, CleanTech One, Singapore 637141, Singapore
[c] School of Civil and Environmental Engineering, Nanyang Technological University, 50 Nanyang Avenue, 639798, Singapore
[d] Division of Chemistry and Biological Chemistry, School of Physical and Mathematical Sciences, Nanyang Technological University, 637371, Singapore
[e] Department of Fundamental and Applied Sciences, Universiti Teknologi PETRONAS, 32610 Seri Iskandar, Perak Darul Ridzuan, Malaysia

ABSTRACT

The thermolytic transformation of lignocellulosic spent coffee grounds to superior redox-active carbocatalyst (denoted as NBC) *via* nitrogen functionalization in a pyrolytic environment at various temperatures was investigated. The intrinsic (*e.g.* surface chemistry, degree of graphitization, *etc.*) and extrinsic (*e.g.* specific surface area, morphology, *etc.*) properties of the catalysts were systematically studied using various characterization techniques. The three main N configurations conducive to redox reactions, namely pyrrolic N, pyridinic N and graphitic N were present at different compositions in all the NBCs prepared at pyrolysis temperature $\geq 500\,°C$. The NBCs were used as peroxymonosulfate (PMS) activator for degrading bisphenol A. It was found that NBC-1000 (prepared at 1000 °C) has the highest catalytic performance ($k_{app} = 0.072\,min^{-1}$) due to the relatively higher specific surface area (438 $m^2\,g^{-1}$), excellent degree of graphitization, and optimum N bonding configuration ratio. Based on the radical scavenger and electron paramagnetic resonance studies, the nonradical pathway involving $^1O_2$ generation is identified as the prevailing pathway while the radical pathway involving $SO_4 \cdot^-$ and $\cdot OH$ generation is the recessive pathway. Further investigation of the durability of surface active sites revealed that the active sites undergo N bonding configuration reconstruction and cannibalistic oxidation (increase in surface oxygen content) during PMS activation reaction. The graphitic N manifest greater catalytic activity and stability compared to pyridinic N and pyrrolic N under oxidizing environment. The results demonstrated that reaction optimization is critical to improve the durability of the catalyst. This study provides useful insights in converting lignocellulosic biomass waste into functional catalytic material, and the strategy to improve the durability of carbocatalysts for redox-based reactions.

1. Introduction

The accelerating global solid waste generation rate presents one of the greatest environmental challenges to date. Specifically, the lignocellulosic biomass wastes are abundant and widely generated in the agricultural and food industries [1]. They can be converted into useful materials for catalytic processes, energy storage and environmental applications. As a typical example of lignocellulosic biomass waste, the spent coffee grounds (SCGs) are generated as residues during brewing process [2]. In 2014, approximately nine million tonnes of SCGs were produced and landfilled [3]. The SCGs have high organic content with main composition consisting of cellulose, hemicellulose and lignin [4]. Such carbonaceous structure can be exploited as a potential low-cost carbon precursor to produce functional materials [5,6]. This can contribute to waste reduction, resource recovery/reclamation, minimize waste landfilling, and provide economic benefits.

Environmental remediation technologies based on peroxymonosulfate (PMS) and persulfate activations have increasingly becoming popular. The metal-based catalysts (*e.g.* Co-, Fe- and Mn-based catalysts) are widely reported as highly-efficient catalyst because they are highly conducive to redox reactions [7–10]. However, the metal-based catalysts suffer from sintering and metal leaching problem

---

leading to the irreversible catalytic deactivation reaction [11,12]. Recently, carbon-based materials (*e.g.*, activated carbon, nanodiamonds, graphene and carbon nanotubes) are increasingly reported as a promising class of metal-free, redox-active catalyst for environmental decontamination [13–16]. The carbon-based catalysts are eco-friendly (no metal leaching problem during catalysis), biocompatible, resistant to acids/bases (chemically stable), and versatile (can be easily tuned to have high catalytic efficiency depending on application) [17]. Previously, the carbon-based catalysts have been reported to successfully act as redox-active catalyst to remove recalcitrant pollutants such as bisphenol A [18] and sulfonamide antibiotics [19]. Nitrogen doping is one of the simplest and most effective approaches used to improve the catalytic activity of carbocatalysts. The introduction of N, which contains excessive valence electrons, on the graphitic structure increases the π electron density in the graphitic plane and enhances the surface reactivity of the catalyst [20]. The most common redox-active N bonding configurations in N-doped carbon catalyst are graphitic N (or quaternary N), pyrrolic N and pyridinic N [19]. These N bonding configurations are sp^2 hybridized, making them extremely reactive for redox-based catalysis. The redox-active N functional groups can be easily coalesced into the carbon lattice by a facile thermolytic process in the presence of N and carbon precursors. To date, the common carbon precursors used (*e.g.*, graphene oxide, carbon nanotubes) for carbocatalyst preparation are considerably expensive and difficult for scale-up. Hence, the use of low-cost carbon precursor such as the lignocellulosic biomass waste is desirable.

It is well documented in the literature that the N-doped carbon catalysts have poor durability as PMS activator for environmental decontamination [14,19,21]. During PMS activation, the catalyst may undergo reconstruction and cannibalistic oxidation of active sites in the highly-oxidizing environment leading to the deactivation of active functional groups conducive to redox reaction. Hence, the investigation of the durability of surface active sites during catalysis is important to provide deeper insights of the deactivation phenomenon. By unveiling the mechanism of catalyst deactivation, practical application of carbocatalysts as redox-active catalyst for PMS activation can be realized.

In this study, SCG was used as precursor to produce N-doped biomass-derived carbon catalyst (denoted as NBC) for PMS activation. The intrinsic (*e.g.*, surface chemistry, degree of graphitization, *etc.*) and extrinsic (*e.g.*, specific surface area, morphology, *etc.*) properties of NBCs produced at different pyrolytic temperatures (T_p) were investigated using various characterization techniques including X-ray diffractometer, X-ray photoelectron spectroscopy, Raman spectroscopy, and porosimeter to identify the optimum operational condition in order to produce high-performance redox-active catalyst. To achieve high catalytic activity, the biomass-derived carbocatalyst must have considerably high degree of graphitization degree and optimum ratios of N configurations to minimize excessive cannibalistic oxidation reactions. For the first time, the durability of the active sites during PMS activation was critically discussed. The study provides useful insights to the conversion of lignocellulosic waste into functional catalytic material and strategy to improve the durability of carbocatalysts for PMS activation.

2. Experimental

2.1. Chemicals

The SCG consisting of irregular dark-brownish particles was obtained from a local coffee shop at Nanyang Technological University (NTU), Singapore. The SCG was washed with deionized (DI) water to remove the soluble fraction, dried in an oven at 100 °C for at least 48 h, and further pulverized to powder form (denoted as SCP, < 100 μm). The SCP was stored in an oven at 60 °C prior to use. The chemicals used in this study were urea (CH_4N_2O, Merck), Oxone® (as $2KHSO_5·KHSO_4·K_2SO_4$, Alfa Aesar), bisphenol A (BPA, $C_{15}H_{16}O_2$, Merck), methanol (CH_3OH, Merck), absolute ethanol (Fisher Chemical), NaN_3 (Merck), nitrobenzene (NB, Merck), 5,5-Dimethyl-1-Pyrroline-*N*-Oxide (DMPO, Cayman Chemical), 2,2,6,6-tetramethylpiperidine (TEMP, Merck) and NaOH (Schedelco). All the chemicals were of analytical grade and were used without further purification. The milli-Q DI water with a resistivity of 18.2 MΩ cm was employed in all the experiments.

2.2. Preparation of NBCs

The NBCs were prepared using a facile pyrolysis process of SCP at selected pyrolysis temperature (T_p). In a typical run, exactly 400 mg of SCP and 2.0 g of urea were mixed homogeneously in an agate mortar. The SCP-urea mixture was transferred to a quartz boat, and then into a horizontal tubular furnace operated under nitrogen atmosphere (the nitrogen flow rate was 250 mL min^{-1}). The furnace was gradually heated at a heating rate of 10 °C min^{-1} to desired T_p and maintained for 1 h. After the pyrolysis process, the catalyst was naturally cooled to room temperature (25 ± 1 °C) under nitrogen atmosphere. At the end of the synthesis, a black powder (denoted as NBC-X, where X represent T_p) was obtained. The NBC was washed several times with DI water to remove soluble fraction and dried in an oven at 60 °C. The NBCs were then transferred into a sealed tube for storage prior to use. The T_p was varied between 300–1000 °C. The holding time was also varied (at $t = 1$, 5 and 10 h) for selected NBC. The schematic illustration of the preparation process is shown in Fig. 1.

2.3. Characterization

The crystallographic structures of SCP and NBCs were determined by obtaining the XRD patterns using X-ray diffractometer (model Bruker AXS D8 Advance) equipped with high-intensity monochromatic
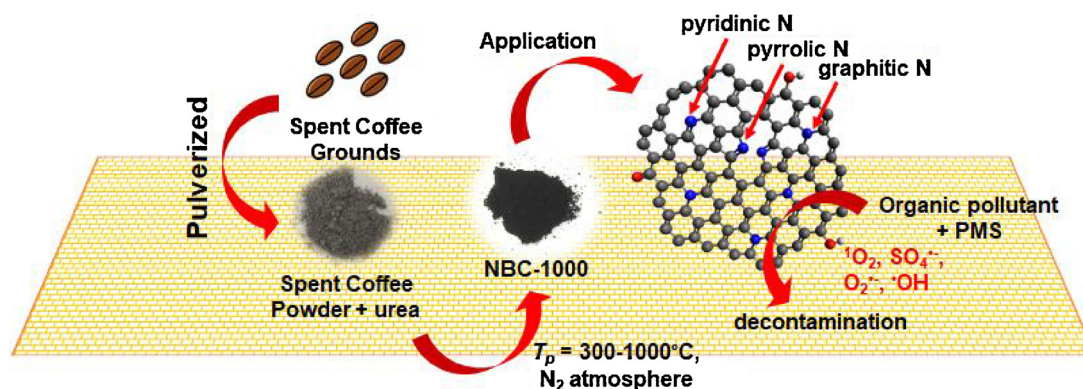

Fig. 1. Schematic illustration of the synthesis of NBC for redox-based catalysis.
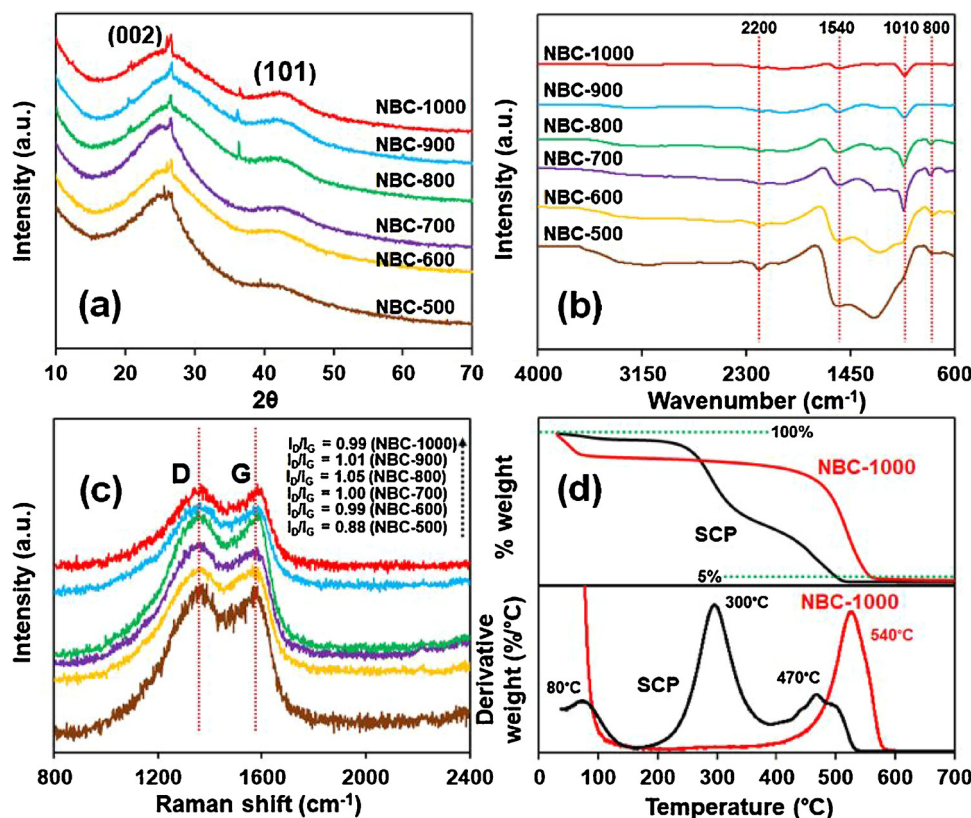
Fig. 2. (a) XRD patterns, (b) FTIR spectra and (c) Raman spectra of NBCs, and (d) TGA and DTG of SCP and NBC-1000.

Cu-Kα source (λ = 1.5218 Å). The scan rate and 2θ range were $0.02°\,s^{-1}$ of 10–70°, respectively. The attenuated total reflectance Fourier transform infrared (FTIR) spectroscopy (Frontier ATR-FTIR, Perkin Elmer) was used to investigate the type of surface functional groups on SCP and NBCs. The Raman spectra of NBCs were obtained using a Raman spectroscopy (XploRA PLUS, Horiba Scientific, Japan) using a 532-nm laser. The surface morphology was studied using a field emission scanning electron microscopy (FESEM, JEOL 7600F) and transmission electron microscopy (TEM, JEM-1400 Plus). The energy dispersive X-ray spectroscopy (EDX, Oxford Xmax80 LN_2 Free) was used to record the EDX spectra of SCP and NBCs. The textural characteristics (specific surface area, average pore size and average pore volume) of SCP and NBCs were investigated by examining the N_2 adsorption-desorption isotherms obtained using a surface area analyser (77 K, Quantachrome Autosorb-1 Analyzer). The CHNS elemental analyser (Elementar, Germany) was used to estimate the elemental composition of SCP and NBCs. The thermogravimetric analysis (TGA) was conducted using a thermogravimetric analyser (PerkinElmer, TGA − 4000). The TGA analysis was carried out at the ramping rate of 10 °C min^{-1} under artificial air atmosphere at 50 mL min^{-1}. The X-ray photoelectron spectroscopy (XPS, Kratos Axis Supra spectrometer) equipped with a dual anode monochromatic Kα excitation source was used to record the XPS spectra of SCP and NBCs. The binding energies of all the elements were corrected against the adventitious carbon C1s core level at 284.8 eV. The deconvolution of the XPS spectra was conducted in the Shirley background together with the Gaussian-Lorentzian function using CASA XPS software. The electron paramagnetic resonance (EPR) spectra was obtained using an EPR spectroscopy (Bruker Biospin ELEXSYS II E500) in continuous wave X-band mode. The spin-trapping agents used were DMPO for trapping $SO_4\cdot^{-}$, $\cdot$OH, and $O_2\cdot^{-}$, and TEMP for trapping $^1O_2$. Analysis of the EPR spectra was conducted using the spin-fitting package of Bruker Xeon software.

2.4. Performance as redox catalyst and durability of active sites

The performances of SCP and NBCs were evaluated as PMS activator for aqueous BPA removal. Briefly, a 100-mL solution containing 5 mg L^{-1} BPA and 0.30 g L^{-1} Oxone® was prepared in a reaction vessel. Then, 20 mg of catalyst (corresponding to 0.20 g L^{-1}) was added into the reaction vessel at 25 ± 1 °C followed by vigorous stirring using a magnetic stirrer to initiate the catalytic reaction. At the end of the reaction ($t = 60$ min), the solution was centrifuged to separate the catalyst from the supernatant. The BPA concentrations before the addition of catalyst and at $t = 60$ min were analysed using a high-performance liquid chromatography (HPLC, Perkin Elmer) and the BPA removal efficiency was calculated as follows:

$$BPA\ removal\ efficiency\ (\%) = \frac{[BPA]_{t=0} - [BPA]_{t=60\,min}}{[BPA]_{t=0}} \times 100\% \quad (1)$$

The HPLC operating condition was as follows: isocratic elution, Hypersil gold C18 reverse phase column, mobile phase = 60% methanol and 40% DI water, flow rate = 0.6 mL min^{-1} and λ_{max} = 220 nm. For selected catalyst and condition, the BPA removal efficiency at other time intervals was also determined. Several operating conditions such as pH (adjusted using 0.1 M NaOH), and Oxone® dosage were also varied. Meanwhile, the used catalysts (for NBC-600 and NBC-1000) were collected and dried in an oven at 60 °C. The XPS spectra of the used catalysts were collected to study the durability of surface actives sites. The XRD pattern of selected used catalyst was also collected to investigate the changes in crystal structure after reaction. For NBC-1000, the used catalyst was resuspended into a fresh solution containing BPA and Oxone® following the similar procedure as described above to investigate the durability of the catalyst. The possible main reactive oxygen species was also investigated using ethanol, NB and NaN$_3$ as radical scavengers for $\cdot$OH, $SO_4\cdot^{-}$ and $\cdot$OH, and $O_2\cdot^{-}$, respectively. The experiment was conducted by following the above-mentioned procedure except that a chemical scavenger was introduced

Table 1
The textural characteristics, %w/w N (CHNS), and %at. N (XPS) configurations of SCP and NBCs.

Catalyst	Specific surface area $(m^2 g^{-1})$	Average pore radius (Å)	Total pore volume $(cm^3 g^{-1})$	%w/w N (CHNS)	%at. Pyrrolic N (XPS)	%at. Pyridinic N (XPS)	%at. Graphitic N (XPS)
SCP	0.3	18.1	0.00	2.1	–	–	–
NBC-500	23.3	16.4	0.06	19.3	46.43	48.67	4.89
NBC-600	23.4	18.2	0.07	16.6	41.85	46.63	11.52
NBC-700	28.8	16.3	0.07	15.0	39.31	45.51	15.19
NBC-800	287.1	18.2	0.10	7.3	44.12	36.56	19.33
NBC-900	295.3	20.4	0.10	5.5	40.25	28.20	31.55
NBC-1000	438.8	18.2	0.16	2.8	32.22	21.30	46.48

into the reaction vessel before the initiation of the experiment. Each of the experiments were conducted in triplicate and the results are reported as averages of three runs.

3. Results and discussion

3.1. Characterization of catalysts

The thermolytic transformation of SCP and urea as carbon and N precursors, respectively, under pyrolytic condition was studied up to 1000 °C. At $T_p = 1000$ °C, the %w/w yield of NBC, which was calculated by the %w/w difference between the as-obtained NBC and SCP precursor, was ~15–21%. The changes in %w/w were attributed to the loss of moisture, volatile organics and non-condensable gases [22]. Considering the decreasing relationship between %w/w yield of NBC and T_p, it is expected that $T_p > 1000$ °C would result in low %w/w yield and this condition is not suitable for producing NBC. The XRD patterns of NBCs prepared at $T_p \geq 500$ °C are presented in Fig. 2a, whereas the XRD patterns for SCP and NBCs prepared at $T_p \leq 400$ °C are shown in Fig. S1a. Several relatively broad diffraction peaks between $2\theta = 15$–$22°$ are observed in the XRD pattern of SCP, which is consistent with the XRD pattern of typical lignocellulosic material [23]. It is observed that $T_p \geq 400$ °C is required to coalesce nitrogen into the carbon lattice of SCP. The XRD pattern of NBC-300 consists of multiple distinctive peaks due to the polycondensation of urea to crystalline phases such as cyanuric acid, melamine and carbon nitride. With thermal treatment at $T_p \geq 400$ °C, two broad diffraction peaks at $2\theta = 26°$ and $42°$, corresponding to (002) and (101) planes, emerged in the XRD patterns indicating thermolytic transformation of SCP to carbonaceous amorphous material. At $T_p \geq 800$ °C, several sharp and distinct peaks appear at $2\theta = 27°$ and $36°$ (Fig. 2a) suggesting the presence of crystalline minerals in the NBCs.

The FTIR spectroscopy was used to investigate the changes of surface functional groups during thermolytic transformation and N-doping. Fig. 2b shows the FTIR spectra of NBCs ($T_p \geq 500$ °C), while the FTIR spectra for SCP and NBCs ($T_p \leq 400$ °C) are presented in Fig. S1b. In the FTIR spectra for SCP, various peaks can be observed, including those at 1020, 1360–1450, 1640–1730, 2850, 2920, and 3350 cm^{-1}, which can be ascribed to C−O (in C−O−H) stretching vibration, C−H bending, C=O, C−H asymmetric and symmetric stretching, aliphatic C−H stretching, and −OH, respectively [24,25]. These functional groups are typical of lignocellulosic biomass which consists of predominantly cellulose, hemicellulose and lignin [26]. At $T_p = 300$ °C, the SCP undergoes carbonization to porous carbon, while urea undergoes polycondensation reactions to cyanuric acid, melamine and carbon nitride, giving rise to the emergence of various peaks at 2800–3200, 1690, 1450–1400 and 760 cm^{-1}. These peaks can be ascribed to the N-based moieties such as −NH$_2$, N−H bending, C−N stretching, and N−H out of plane bending, respectively [27,28]. The N-based moieties are decomposed and coalesced into the carbon lattice at $T_p \geq 400$ °C to form various N configurations including pyridinic N, pyrrolic N and graphitic N. It is observed that the intensities of peaks between 900–1700 cm^{-1} decreases along with the emergence of a peak at

1010 cm^{-1} (which can be ascribed to C−O) at $T_p \geq 700$ °C (Fig. 2b). This is due to (i) thermolytic decomposition of oxygen-containing carbonaceous components which exposes more C−O groups [29], (ii) decomposition of pyridinic N and pyrrolic N which are less thermostable than graphitic N [30], and (iii) thermal restructuring of pyridinic N to graphitic N [31] in the porous carbon.

Fig. 2c shows the Raman spectra of NBCs ($T_p \geq 500$ °C). The D and G bands are observed ($T_p \geq 500$ °C) at ~1390 and ~1600 cm^{-1}, respectively. The D (related to the K-point phonons of A$_{1g}$ symmetry) and G (related to the zone centre phonons of E$_{2g}$ symmetry) bands in the Raman spectra of carbonaceous materials can be used to characterize the structural features such as degrees of surface defects and disorder [32]. The ratio of peak heights of D and G bands (I_D/I_G) is closely correlated to the degree of disorder of the catalyst. A higher I_D/I_G ratio indicates higher degree of disorder density. The I_D/I_G ratio increased gradually from 0.88 at $T_p = 500$ °C to 1.05 at $T_p = 800$ °C indicating increasing defective sites density and edge plane exposures from N doping. The formation of pyridinic N and pyrrolic N at $T_p = 500$ °C, which are p-type dopants, promotes upshift of G peak. With increasing T_p up to 800 °C, the pyridinic N and pyrrolic N gradually decomposed and the graphitic N content, which is the n-type dopant, increased, and this induced downshift of the G peak [19]. However, the I_D/I_G ratio decreased from 1.05 to 0.99 with further increase in T_p from 800 to 1000 °C and this could be due to the gradual increase in graphitization degree of NBC. The higher T_p also leads to the decomposition of amorphous carbon which is less thermostable than graphitic carbon [33].

Table 1 shows the textural characteristics of SCP and NCBs. The S_{BET} of SCP increased ~100 times from 0.3 $m^2 g^{-1}$ to ~23–29 $m^2 g^{-1}$ at T_p between 500–700 °C. The increment in S_{BET} is due to the progressive conversion of SCP (constituting hemicellulose, cellulose and lignin) to porous carbon accompanied by the loss of volatile organics [34]. Further increase of T_p from 700 °C to 1000 °C resulted in a dramatic increase of S_{BET} and total pore volume up to 439 $m^2 g^{-1}$ and 0.16 $cm^3 g^{-1}$, respectively. This is attributed to the partial decomposition of amorphous carbon, and conversion of the amorphous carbon to denser graphitic carbon, leading to the formation of meso- and micro-porous networks [35]. The larger S_{BET} and lower amorphous carbon content are important in catalytic advanced oxidation processes to provide better catalyst-substrate contact and reduce potential ROS scavenging, respectively.

The microstructural features of SCP and NBC-1000 were investigated using the FESEM and TEM (Fig. 3). The SCP consists of irregular microparticles with considerably smooth surface, while the NBC-1000 can be observed as microparticles with rough surface texture consisting of semi-crystalline carbon. The incorporation of N heteroatoms into the carbon lattice can increase the degree of disorder of carbon, increasing surface defects, which often exists at the edge. This leads to the formation of wrinkles and pores on the microstructural features of the NBC-1000 which is consistent with the characteristic morphology of N-doped carbon [36]. Fig. 3d shows the EDX spectra of NBC-1000 indicating the presence of small amount of trace minerals, namely Mg, Ca, K and P despite throughout washing protocol. In
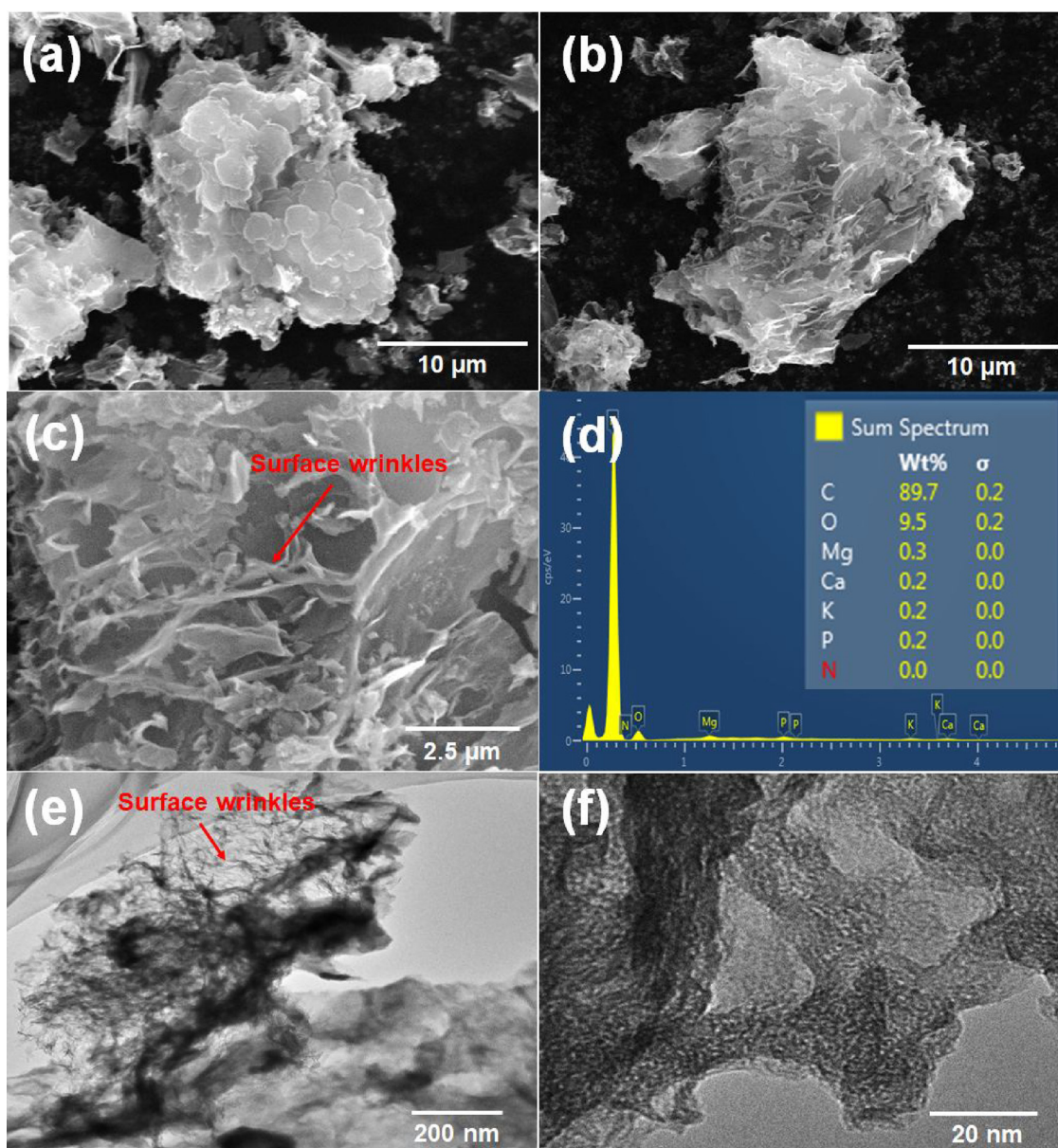
Fig. 3. FESEM micrographs of (a) SCP, (b and c) NBC-1000, EDX spectra of NBC-1000, and TEM micrographs (e and f) of NBC-1000.

general, these trace minerals are not known to be conducive to redox-based reactions. They are present at low concentration (< 4% of total mass of SCP) and can form other crystalline phases (such as whitlockite) or trapped in the NBCs during thermolytic process [37,38]. The N was not detected in the EDX analysis and this could be due to the lower EDX detection limit, and overlapping Kα peaks of C and N. The TGA can be used to quantify the amount of trace minerals in the SCP and NBC-1000. Fig. 2d shows the TGA and differential thermogravimetric (DTG) curves of SCP and NBC-1000. The %wt. of residues (ashes) of SCP and NBC-1000 were < 4%. The differential thermogravimetric (DTG) curve of SCP indicates that three distinct peaks were present corresponding to the loss of water (80 °C), hemicellulose (300 °C), and cellulose + lignin (470 °C), respectively [39]. The DTG curve of NBC-1000 consists of two characteristics peaks at 80 °C (water loss) and 540 °C further supporting the conversion of the lignocellulosic structure to semi-crystalline carbon material with higher thermal stability.

To further evaluate the compositions and chemical states of SCP and NBCs, the CHNS elemental composition and XPS survey spectra were obtained. The N/C and O/C ratios for NBCs, calculated from the XPS spectra and CHNS elemental analyses, are shown in Fig. 4a. Based on the CHNS analysis, the SCP should consist of 2.1 wt.% N but there was no N signal detected in the corresponding XPS survey spectrum due to the relatively low specific surface area (and poor N surface coverage) of SCP. This suggests that N is likely embedded in the lignocellulosic structure. While the NBC prepared at $T_p \leq 300$ °C has the highest N content with N/C (CHNS) > 0.75, the N exists mainly as surface impurities because $T_p \leq 300$ °C is inadequate to provide sufficient energy for N to coalesce into the carbon lattice (consistent with the characterization results above). It is observed that the O/C (XPS) increased gradually from 0.05 to 0.15, and then decreased progressively to 0.06 with further increase in T_p from 800 to 1000 °C. This is different from the observed O/C (CHNS) trend which decreased progressively with increasing T_p. This means that at $T_p \leq 700$ °C, the thermolytic decomposition of lignocellulosic structure resulted in higher exposed surface oxygen groups but at the expense of the total oxygen content. The result is substantiated by the FTIR spectra which indicates the emergence of new oxygen functional groups (C─O moiety) at $T_p = 700$ °C (Fig. 2b). However, with further increase in T_p, the C─O moiety decomposed due
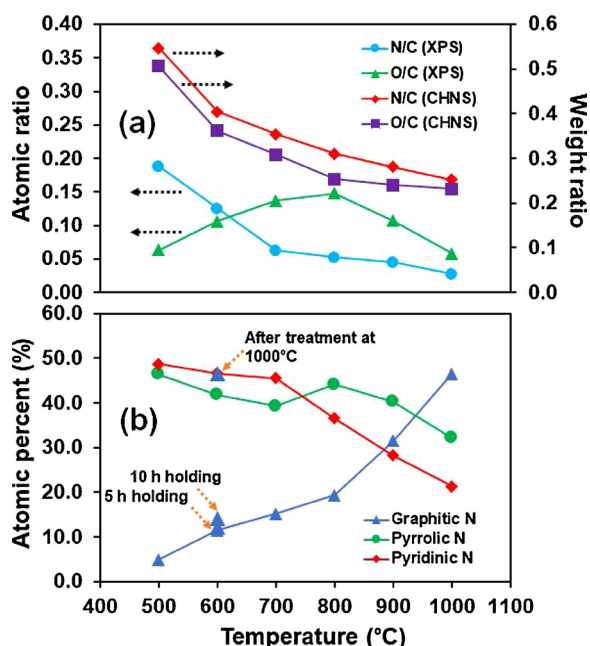
Fig. 4. The variations of (a) O/C and N/C contents, and (b) N bonding configurations for NBCs prepared at different T_p.

to higher degree of carbonization as evidenced by the decreasing trend of FTIR peak at 1010 cm^{-1}. Similarly, the N/C (CHNS) and N/C (XPS) decreased progressively with increasing T_p from 500 to 1000 °C due to the thermal decomposition and carbonization of the NBC structure.

The catalytic activity of NBC is dependent on the types of N bonding configurations present on NBC, whereby an optimum ratio of various N bonding configurations can promote adsorption and catalytic reactions [40]. To clearly follow the transformation of N bonding configurations with T_p, high-resolution XPS spectra in the N1s region of NBCs were obtained (Fig. S2). All the N1s XPS spectra can be deconvoluted into three main peaks at binding energies of ~398, ~401 and ~403 eV, corresponding to pyridinic N, pyrrolic N and graphitic N, respectively. The calculated at.% of each N bonding configuration is presented in Fig. 4b. In NBCs prepared at T_p = 500–700 °C, the pyrrolic N and pyridinic N are dominant (at least 40 at.% of total N) while graphitic N only accounted for < 15 at.% of total N. With the progressive increase in T_p from 700 to 1000 °C, the at.% of pyrrolic N and pyridinic N decreased, while at.% of graphitic N increased drastically up to 46 at.%. This is attributed to the lower thermal stabilities of pyrrolic N and pyridinic N, which are decomposed at higher T_p compared to graphitic N which has higher thermal stability [19,41]. The decomposition of pyrrolic N and pyridinic N leads to the decrease in total wt.% N in the NBC. The effect of holding time on the composition of N bonding configuration was also studied for NBC-600. The results show that the holding time up to 10 h has no significant effect on the composition of N bonding configurations and N/C (XPS) (~0.13–0.14) (Fig. S3). However, when NBC-600 was subjected to thermal treatment at 1000 °C, the composition of N bonding configurations in NBC-600 are modulated to be similar to that of NBC-1000 indicating that T_p is the key parameter in controlling the N bonding configurations in the NBC.

3.2. Performance evaluation

Fig. 5 compares the performance of various NBCs as PMS activator for BPA degradation. The BPA was selected as the model pollutant because it is an endocrine disruptor of great human health concern and omnipresent in the aqueous ecosystem [42,43]. The catalytic reaction was evidenced in the control study whereby the BPA did not react favourably with PMS alone (< 2% BPA removal, 0.30 g L^{-1} Oxone®). The
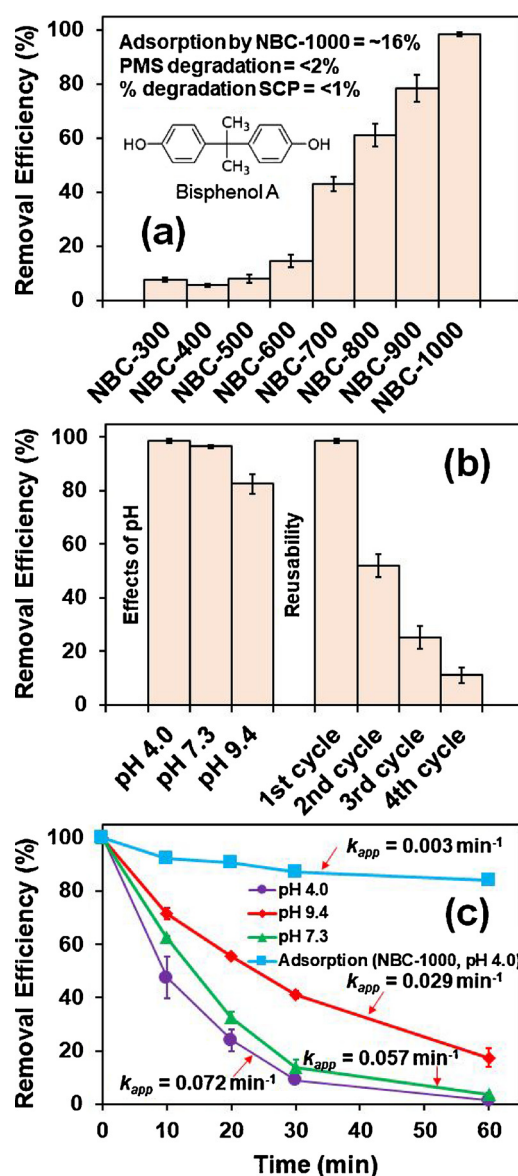

Fig. 5. (a) The performance of SCP and NBCs for BPA degradation *via* PMS activation, (b) Effect of pH on BPA removal efficiency, and NBC-1000 durability, and (c) Comparison of BPA removal efficiency at various pHs. (Conditions: [BPA] = 5 mg L^{-1}, [Oxone®] = 0.30 g L^{-1}, [catalyst = 0.20 g L^{-1}], reaction time = 60 min (for a and b), and pH = 4.0 for (a) and durability study).

adsorption by NBC-1000 contributed to ~16% of BPA removal which could be induced by the π–π interactions between BPA and surface functional groups of NBC-1000 [44]. The SCP showed only ~1% BPA degradation with PMS under the same conditions. The NBCs prepared at T_p ≤ 600 °C have low catalytic activity (< 20%) and this could be attributed to (i) the presence of excessive active sites from N doping (mainly pyridinic N and pyrrolic N), (ii) high amorphous carbon content, and (iii) relatively lower specific surface area compared to NBCs prepared at T_p ≥ 700 °C. The first two factors can cause PMS and ROS scavenging, reducing the available PMS and ROS for efficient BPA degradation. From T_p = 700 °C, the catalytic activity increased linearly from 43 ± 3% to 99 ± 1% at T_p = 1000 °C concomitant with the gradual increase of graphitic N (and decrease in surface defects, pyridinic N and pyrrolic N), decrease in the amorphous carbon content, and increase in the specific surface area. The BPA degradation of NBC-1000 follows the pseudo first-order kinetics with apparent first-order
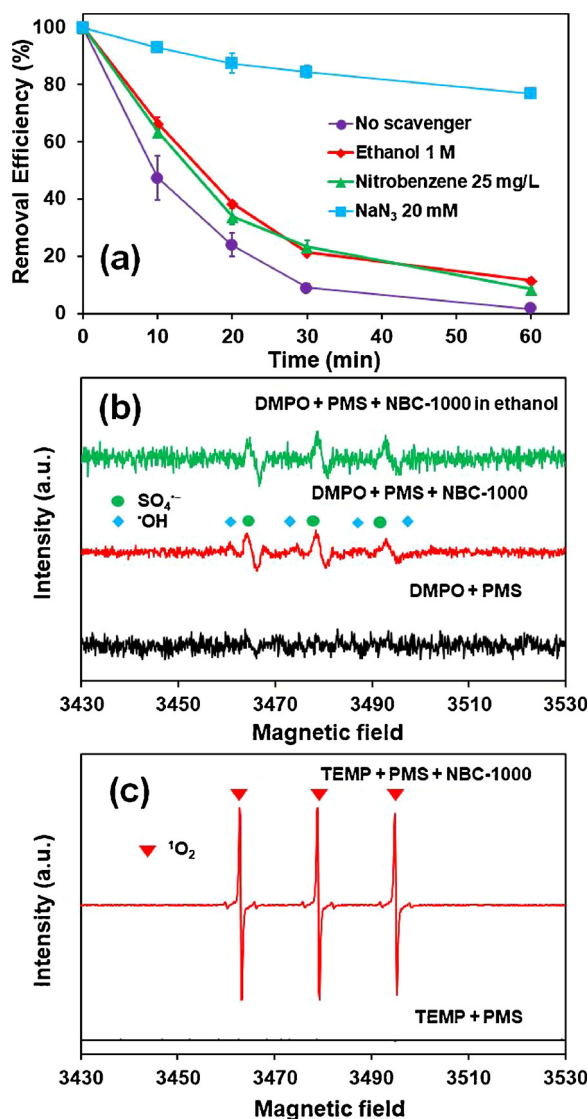
Table 2
The changes in O/C (XPS), N/C (XPS), O/N ratio, and pyrrolic N/pyridinic N atomic ratio for NBC-600 and NBC-1000 before and after oxidation reactions.

Catalyst	O/C (XPS)	N/C (XPS)	O/N (XPS)	Pyrrolic N/Pyridinic N atomic ratio
NBC-600	0.11	0.12	0.9	0.89
NBC-600 (used)–pH 4.0	0.24	0.02	12.0	0.89
NBC-1000	0.06	0.027	2.2	1.51
NBC-1000 (used)–pH 4.0	0.11	0.022	5.0	1.57
NBC-1000 (used)–pH 7.3	0.10	0.026	3.8	1.60
NBC-1000 (used)–pH 9.4	0.07	0.03	2.3	1.89

rate constant, k_{app} = 0.072 min^{-1}). Since NBC-1000 has the highest catalytic activity, it was selected to study the effect of pH on BPA degradation and durability of the catalyst. As indicated in Fig. 5c, the BPA removal rate decreased gradually from 0.072 to 0.029 min^{-1} with increasing pH from 4.0 to 9.4 due to the occurrence of surface repulsion at higher pH (particularly at pH 9.4) between the negatively charged NBC-1000 (pH$_{pzc}$ = 7.4) surface, BPA (pK_a = 9.6–10.2) and PMS (pK_{a2} = 9.4), hindering the catalytic reaction [45,46]. Meanwhile, in the durability study, the BPA removal efficiency decreased from 99 ± 1% to 52 ± 4%, 25 ± 1% and 11 ± 3% for second, third and fourth cycle, respectively. The decrease in the BPA removal efficiency could be attributed to several factors including the N configuration reconstruction, cannibalistic surface oxidation, and sorption of organics on catalyst surface during PMS activation process, which decreases the density of active sites available for PMS activation.

3.3. Identification of main ROS

Since BPA degradation in PMS/NBC-1000 system can occur through radical and nonradical pathways, it is imperative to identify the main BPA oxidation pathway and ROS generated in the system. Two methods were used, namely (i) indirect method using radical scavengers (ethanol, NB and NaN$_3$), and (ii) direct method using EPR spectroscopy with spin trapping agents (DMPO and TEMP). Fig. 6a shows the influence of selected radical scavengers on BPA removal rate. Ethanol was used as $SO_4\cdot^-$ and $\cdot OH$ scavenger because it has considerably high reaction rate with $SO_4\cdot^-$ ($k_{SO_4^{\cdot-}+EtOH}$ = 1.6 × 10^7 M^{-1} s^{-1}) and $\cdot OH$ ($k_{\cdot OH+EtOH}$ = 1.9 × 10^9 M^{-1} s^{-1}) [17]. NB is a suitable $\cdot OH$ scavenger because it has a considerably high reaction rate with $\cdot OH$ ($k_{\cdot OH+NB}$ = 3.9 × 10^9 M^{-1} s^{-1}) but low reaction rate with $SO_4\cdot^-$ ($k_{SO_4^{\cdot-}+NB}$ < 10^6 M^{-1} s^{-1}). As indicated in Fig. 6a, the addition of ethanol and NB did not result in significant inhibition to the BPA degradation (< 10% difference in BPA removal efficiency at t = 60 min) implying that the oxidation reaction was not dominated by radical pathway involving $SO_4\cdot^-$ and $\cdot OH$. The addition of NaN$_3$ as a $^1O_2$ radical scavenger resulted in a significant inhibition to the BPA degradation. While other studies have used NaN$_3$ as $^1O_2$ radical scavenger for other systems [28,47], it should be noted that NaN$_3$ cannot be used to exclusively confirm the contribution of $^1O_2$ as the dominant ROS in the PMS/NBC-1000 since it can react with PMS and other ROS (such as $SO_4\cdot^-$ and $\cdot OH$) [48].

To further probe the main ROS generated in the PMS/NBC-1000 system, spin trapping agents, namely DMPO and TEMP, were employed to trap the generated ROS for subsequent detection with EPR. As shown in Fig. 6b, the EPR spectrum of PMS/NBC-1000 system (with DMPO as the spin trapping agent) provide substantial evidence of the presence DMPO adducts at weak intensities, which can be assigned to the DMPO-$SO_4\cdot^-$ and DMPO-$\cdot OH$ adducts [49]. To probe the possibility of $O_2\cdot^-$ as a major ROS, the ROS trapping experiment by DMPO was conducted in absolute ethanol (since the DMPO-$O_2\cdot^-$ adduct has better stability in

Fig. 6. (a) The effect of selected radical scavengers on BPA degradation, (b) EPR spectra of PMS/NBC-1000 with DMPO spin trapping agent, and (c) EPR spectra of PMS/NBC-1000 with TEMP spin trapping agent. Conditions: [BPA] = 5 mg L^{-1}, [Oxone*] = 0.30 g L^{-1}, [catalyst = 0.20 g L^{-1}], pH = 4.0, reaction time (for b and c) = 1 min, [DMPO] = 80 mM and [TEMP] = 80 mM.
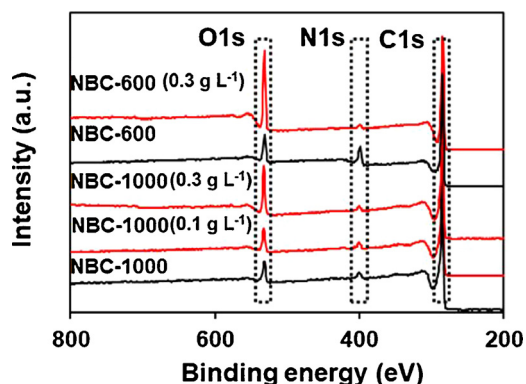

Fig. 7. XPS survey scan of NBC-600 and NBC-1000 before and after use. (Conditions: [BPA] = 5 mg L^{-1}, [Oxone*] = 0.30 or 0.10 g L^{-1}, [catalyst = 0.20 g L^{-1}], reaction time = 60 min).
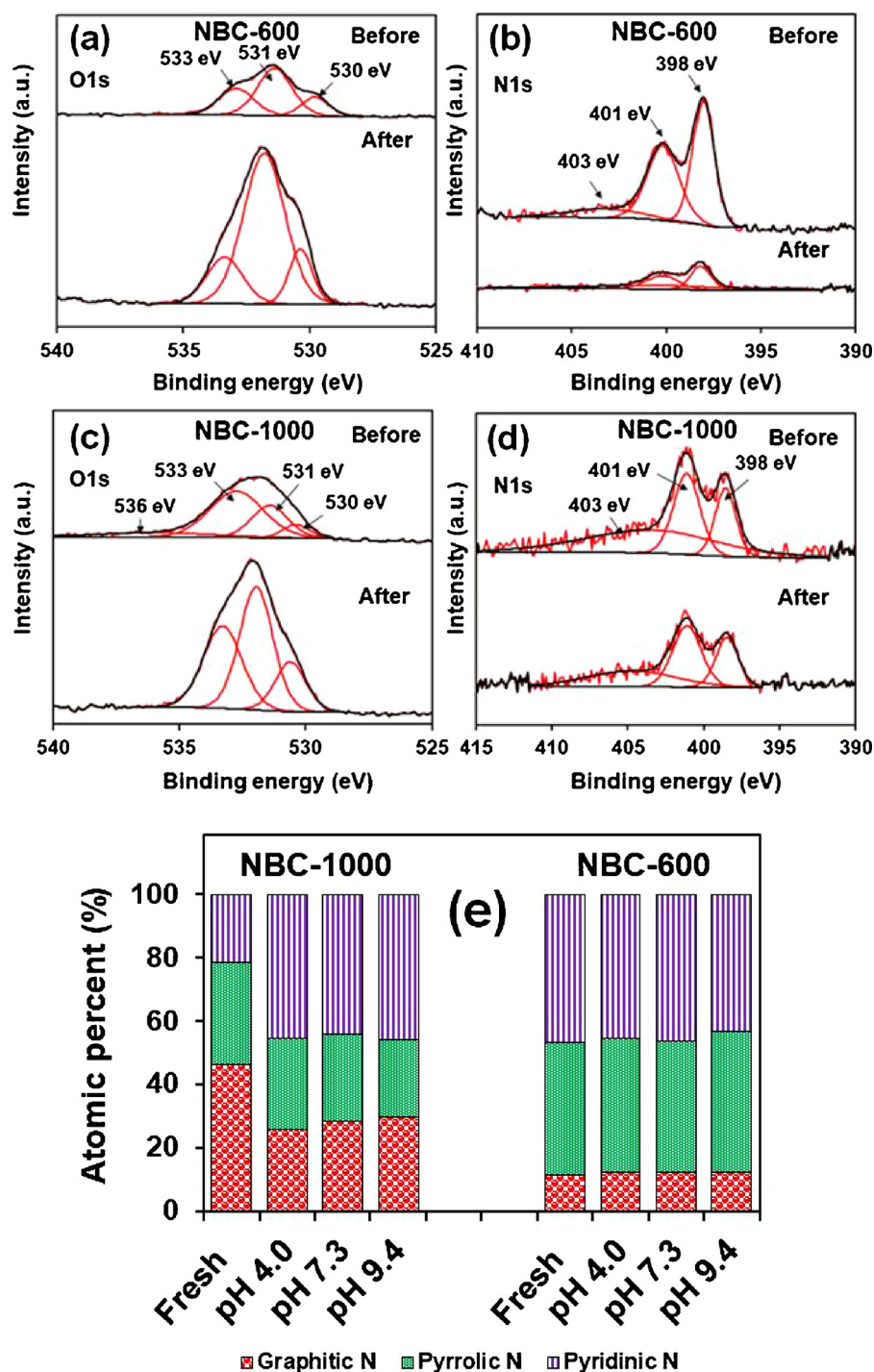
Fig. 8. High resolution XPS spectra of NBC-600 (a and b) and NBC-1000 (c and d) at the O1s and N1s regions, and (e) changes in the N surface functional groups before and after used. (Conditions: [BPA] = 5 mg L^{-1}, [Oxone$^{\circ}$] = 0.30 g L^{-1}, [catalyst = 0.20 g L^{-1}], reaction time = 60 min, and pH = 4.0 for (a)–(e)).

absolute ethanol). However, there was no significant increase in the DMPO-O$_2$·$^-$ adduct signal in the EPR spectrum further suggesting that O$_2$·$^-$ is unlikely to be the main ROS generated in the system. When TEMP was employed as the spin trapping agent, very strong signals (hyperfine splitting constants of a^N = 16 G, relative intensity ratio of 1:1:1), which can be assigned to 2,2,6,6-tetramethyl-4-piperidone-*N*-oxyl radical (TEMPO), were detected, providing strong evidence that ^{1}O$_2$ was the primary ROS generated in the PMS/NBC-1000 system. This is not surprising considering NBC-1000 is rich in graphitic N, acting as a possible active site for ^{1}O$_2$ generation through nucleophilic addition of

PMS in the nonradical oxidative pathway. However, the results merely mean that ^{1}O$_2$ is the primary ROS generated in the reaction system and the contribution of O$_2$·$^-$ to BPA degradation cannot be excluded entirely since O$_2$·$^-$ can be produced from ^{1}O$_2$ [50]. Meanwhile, other active sites conducive to redox reaction and vital for radical pathway (i.e. pyrrolic N and pyridinic N) are also present to facilitate the formation of ROS, albeit at a lower quantum. Hence, the nonradical pathway involving ^{1}O$_2$ generation is the prevailing pathway while radical pathway involving SO$_4$·$^-$ and ·OH is the recessive pathway.
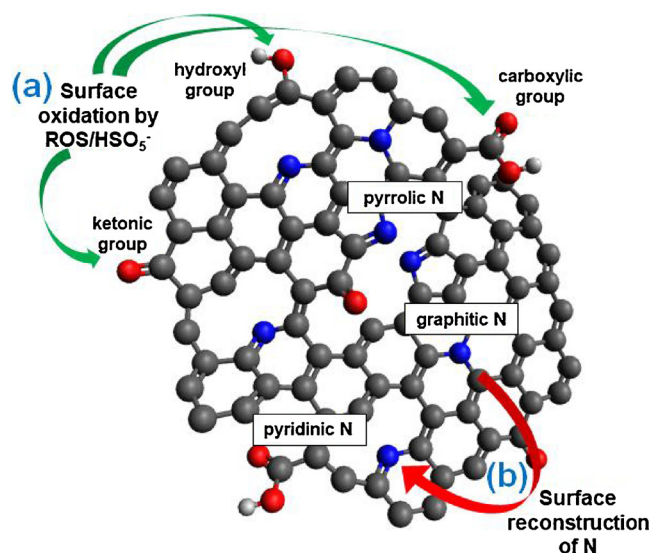
Fig. 9. Proposed mechanism of catalyst deactivation involving (a) surface oxidation and (b) reconstruction of surface N bonding configurations.

3.4. Durability of surface active sites

The XRD pattern after the catalytic reactions was also obtained (Fig. S4) indicating that there is no significant change in the crystallographic structure of NBC-1000. To further probe the changes in the surface-active sites of NBCs, XPS survey scan and before and after the catalytic reactions were obtained (Fig. 7). The changes in O/C (XPS), N/C (XPS), O/N (XPS), and pyrrolic N/pyridinic N peak area ratio for NBC-600 and NBC-1000 before and after oxidation reactions are tabulated in Table 2. There is no interference of N from the pollutant to the N1s XPS spectra since BPA has no N. It is observed that the O/C (XPS) increased from 0.06 to 0.11 and 0.11 to 0.24 for NBC-1000 and NBC-600, respectively, after the catalytic process, providing conclusive evidence that the oxidation reactions by PMS and the generated ROS ($^1O_2$, $O_2 \cdot^-$, $SO_4 \cdot^-$ and $\cdot OH$) occurred on the catalyst surface. This is not surprising considering PMS is a strong oxidant and was previously used to increase the surface oxygen content of carbon materials [51]. The high-resolution XPS spectra of fresh and used NBC-600 and NBC-1000 in the N1s and O1s regions were obtained to further understand the impact of the surface oxidation reactions (Fig. 8). The O1s spectra of used NBC-600 and NBC-1000 can be deconvoluted into three main peaks at 530, 531 and 533 eV, corresponding to O=C−OH, C=O and C−OH, respectively. The peak at 536 eV corresponding to C−O−C in fresh NBC-1000 was not detected in the used NBC-1000, suggesting decomposition. Compared to the corresponding O1s spectra of fresh catalysts, the higher O/N (XPS) ratio indicate the increase in O=C−OH, C=O, and C−OH moieties, which are the common oxidation products of carbon.

$$\text{Carbon surface} + {}^1O_2/SO_4 \cdot^-/\cdot OH/O_2 \cdot^-/PMS \rightarrow -COOH + -C=O + -C-OH \tag{2}$$
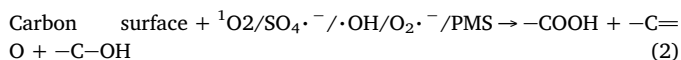
The variation of O/N (XPS) ratio (Table 2) with respect to pH suggests the quantum of surface oxidation was ~2 lower at pH 9.4 compared to that at pH 4.0. The electrostatic effect at basic pH prevents the PMS-catalyst contact, reducing the ROS generation rate, which agrees with the results obtained in the performance studies.

As indicated in Table 2, the N/C (XPS) for NBC-600 decreased drastically from 0.12 to 0.02 (~83% difference) after catalytic reaction indicating rapid decomposition of N bonding configurations, particularly pyridinic N and pyrrolic N, under highly-oxidizing environment. Because pyridinic N and pyrrolic N are all redox-active species conducive to PMS activation particularly via radical pathway [21,52], it is expected that the decomposition of N bonding configurations in NBC-

600 is due to two factors, namely (i) by irreversible redox reaction with PMS, generating ROS ($SO_4 \cdot^-$, $O_2 \cdot^-$ and $\cdot OH$) and consuming the active sites, and (ii) by cannibalistic reactions involving the generated ROS with pyridinic N, pyrrolic N and carbon surface. Comparatively, the N/C (XPS) for NBC-1000 showed significantly lower quantum of decrease from 0.027 to 0.022 after catalytic reaction. Since NBC-1000 has a higher density of graphitic N (and lower densities of pyridinic N and pyrrolic N), this suggests that graphitic N is the main active sites for PMS activation, which manifest greater stability compared to pyrrolic N and pyridinic N in oxidizing environment. Hence, having an optimum ratio of these N bonding configurations with high density of %at. graphitic N is crucial for better catalytic performance. By modulating NBC-600 to have achieve the N-doping configuration ratio of NBC-1000 (with additional thermal treatment at T_p = 1000 °C, 46 at.% graphitic N), 99% BPA degradation was achieved (Fig. S5a).

Interestingly, obvious reconstruction of N bonding configurations can be observed in the used NBC-1000 at all the pHs studied (Fig. 8e). The pyrrolic N/pyridinic N atomic ratio increased from 1.51 (fresh NBC-1000) to 1.57–1.89 after used, along with the decrease in at.% graphitic N as the result of the N bonding configuration reconstruction during PMS activation reaction (Table 2). Such reconstruction suggests that the major mechanism of PMS activation could involve the irreversible conversion of graphitic N to pyridinic N. This phenomenon could be one of the main reasons accounting for the poor durability of carbon-based catalysts as observed in many studies [14,53]. Overall, the proposed mechanism of surface oxidation and N configuration reconstruction is illustrated in Fig. 9.

To restore the graphitic N, post-heat treatment can be employed to revert pyridinic N back to graphitic N [54].

$$\text{Graphitic N} (\xrightarrow{\text{PMS activation}}) \text{pyridinic N} (\xrightarrow{\text{heat treatment}}) \text{Graphitic N} \tag{3}$$
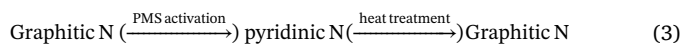
The conversion is feasible but energy consuming since high temperature of at least 800–1000 °C is required for efficient conversion. Furthermore, the thermal treatment may also reduce the total N content of the catalyst [55]. To avoid having to employ frequent thermal treatment to restore the redox-active N bonding configurations, lower Oxone® dosage can be employed. By reducing the Oxone® dosage from 0.30 g L^{-1} to 0.10 g L^{-1}, it was found that the surface oxidation and N bonding configurations reconstruction can be minimized but this comes at the expense of the catalytic performance whereby a decreased in BPA removal efficiency from 99 ± 1 to 42 ± 2% was observed (Fig. S5b). Hence, a delicate process optimization (pH and Oxone® dosage controls) is recommended for improved reaction process and catalyst durability.

4. Conclusions

In summary, SCG was employed as a carbon precursor to prepare N-functionalized carbocatalyst via pyrolysis treatment. The thermolytic transformation of the SCG to NBCs at different temperatures was systematically investigated. The NBCs were used as PMS activator to remove BPA in aqueous system. The NBC prepared at 1000 °C possessed the highest catalytic activity owning to its relatively high surface area, excellent degree of graphitization, and optimum N configurations. The nonradical pathway involving $^1O_2$ generation is determined to be the prevailing pathway while the radical pathway involving $SO_4 \cdot^-$ and $\cdot OH$ generation is the recessive pathway. The durability of the catalyst was investigated. Based on the XPS results, it is proposed that the major PMS activation mechanism could involve the conversion of graphitic N to pyridinic N leading to the N configuration reconstruction. The cannibalistic oxidation reaction resulted in the increase in the oxygen content and destruction of the active sites. The N bonding configuration reconstruction and cannibalistic surface oxidation resulted in the decrease in catalyst durability. The N bonding configuration of used catalyst can be restored with thermal treatment. The lifespan of the carbocatalyst can be prolonged by operating under optimal conditions.

These results envisaged new insights into the use of lignocellulosic biomass waste as a potential carbon precursor to prepare highly-functional catalytic materials, and provided some understanding of the catalytic reaction.

Appendix A. Supplementary data

Supplementary material related to this article can be found, in the online version, at doi:https://doi.org/10.1016/j.apcatb.2018.03.106.

References

[1] J.K. Saini, R. Saini, L. Tewari, 3 Biotech 5 (2015) 337–353.
[2] R. Campos-Vega, G. Loarca-Piña, H.A. Vergara-Castañeda, B.D. Oomah, Trends Food Sci. Technol. 45 (2015) 24–36.
[3] S.K. Karmee, Waste Manage. (Oxf.) 72 (2018) 240–254.
[4] C. Kourmentza, C.N. Economou, P. Tsafrakidou, M. Kornaros, J. Clean. Prod. 172 (2018) 980–992.
[5] Y. Yuan, N. Bolan, A. Prévoteau, M. Vithanage, J.K. Biswas, Y.S. Ok, H. Wang, Bioresour. Technol. 246 (2017) 271–281.
[6] F.R. Oliveira, A.K. Patel, D.P. Jaisi, S. Adhikari, H. Lu, S.K. Khanal, Bioresour. Technol. 246 (2017) 110–122.
[7] Y. Yao, H. Chen, J. Qin, G. Wu, C. Lian, J. Zhang, S. Wang, Water Res. 101 (2016) 281–291.
[8] Y. Yao, C. Lian, Y. Hu, J. Zhang, M. Gao, Y. Zhang, S. Wang, J. Hazard. Mater. 338 (2017) 265–275.
[9] W.-D. Oh, S.-K. Lua, Z. Dong, T.-T. Lim, Nanoscale 8 (2016) 2046–2054.
[10] W.-D. Oh, Z. Dong, G. Ronn, T.-T. Lim, J. Hazard. Mater. 325 (2017) 71–81.
[11] Y. Yao, C. Lian, G. Wu, Y. Hu, F. Wei, M. Yu, S. Wang, Appl. Catal. B: Environ. 219 (2017) 563–571.
[12] W.-D. Oh, V.W. Chang, Z.-T. Hu, R. Goei, T.-T. Lim, Chem. Eng. J. 323 (2017) 260–269.
[13] Q. Zhao, Q. Mao, Y. Zhou, J. Wei, X. Liu, J. Yang, L. Luo, J. Zhang, H. Chen, H. Chen, L. Tang, Chemosphere 189 (2017) 224–238.
[14] X. Duan, Z. Ao, H. Sun, S. Indrawirawan, Y. Wang, J. Kang, F. Liang, Z.H. Zhu, S. Wang, ACS Appl. Mater. Interfaces 7 (2015) 4169–4178.
[15] X. Duan, Z. Ao, L. Zhou, H. Sun, G. Wang, S. Wang, Appl. Catal. B: Environ. 188 (2016) 98–105.
[16] X. Duan, Z. Ao, H. Zhang, M. Saunders, H. Sun, Z. Shao, S. Wang, Appl. Catal. B: Environ. 222 (2018) 176–181.
[17] W.-D. Oh, Z. Dong, T.-T. Lim, Appl. Catal. B: Environ. 194 (2016) 169–201.
[18] W. Ma, N. Wang, Y. Fan, T. Tong, X. Han, Y. Du, Chem. Eng. J. 336 (2018) 721–731.
[19] X. Chen, W.-D. Oh, Z.-T. Hu, Y.-M. Sun, R.D. Webster, S.-Z. Li, T.-T. Lim, Appl. Catal. B: Environ. 225 (2018) 243–257.
[20] W.J. Lee, U.N. Maiti, J.M. Lee, J. Lim, T.H. Han, S.O. Kim, Chem. Commun. 50 (2014) 6818–6830.
[21] G. Wang, S. Chen, X. Quan, H. Yu, Y. Zhang, Carbon 115 (2017) 730–739.
[22] B. Zhao, D. O'Connor, J. Zhang, T. Peng, Z. Shen, D.C.W. Tsang, D. Hou, J. Clean. Prod. 174 (2018) 977–987.
[23] J. Zhang, Y. Wang, L. Zhang, R. Zhang, G. Liu, G. Cheng, Bioresour. Technol. 151 (2014) 402–405.
[24] L. Hao, P. Wang, S. Valiyaveettil, Sci. Rep. 7 (2017) 42881.
[25] L.F. Ballesteros, J.A. Teixeira, S.I. Mussatto, Food Bioprocess Technol. 7 (2014) 3493–3503.
[26] F. Xu, J. Yu, T. Tesso, F. Dowell, D. Wang, Appl. Energy 104 (2013) 801–809.
[27] D.J. Merline, S. Vukusic, A.A. Abdala, Polym. J. 45 (2013) 413–419.
[28] W.-D. Oh, L.-W. Lok, A. Veksha, A. Giannis, T.-T. Lim, Chem. Eng. J. 333 (2018) 739–749.
[29] B. Chen, D. Zhou, L. Zhu, Environ. Sci. Technol. 42 (2008) 5137–5143.
[30] X. Gai, H. Wang, J. Liu, L. Zhai, S. Liu, T. Ren, H. Liu, PLoS One 9 (2014) e113888.
[31] W. Chen, H. Yang, Y. Chen, M. Xia, X. Chen, H. Chen, Environ. Sci. Technol. 51 (2017) 6570–6579.
[32] A.C. Ferrari, J. Robertson, Phys. Rev. B 61 (2000) 14095.
[33] J. Zhao, Y. Liu, X. Quan, S. Chen, H. Yu, H. Zhao, Appl. Surf. Sci. 396 (2017) 986–993.
[34] X. Wang, W. Zhou, G. Liang, D. Song, X. Zhang, Sci. Total Environ. 538 (2015) 137–144.
[35] L. Zhao, W. Zheng, X. Cao, Chem. Eng. J. 250 (2014) 240–247.
[36] F. Razmjooei, K.P. Singh, M.Y. Song, J.-S. Yu, Carbon 78 (2014) 257–267.
[37] P. Pohl, E. Stelmach, M. Welna, A. Szymczycha-Madeja, Food Anal. Methods 6 (2013) 598–613.
[38] H. Li, X. Dong, E.B. da Silva, L.M. de Oliveira, Y. Chen, L.Q. Ma, Chemosphere 178 (2017) 466–478.
[39] H. Yang, R. Yan, H. Chen, D.H. Lee, C. Zheng, Fuel 86 (2007) 1781–1788.
[40] X. Wang, Y. Qin, L. Zhu, H. Tang, Environ. Sci. Technol. 49 (2015) 6855–6864.
[41] S. Zhang, S. Tsuzuki, K. Ueno, K. Dokko, M. Watanabe, Angew. Chem. Int. Ed. 54 (2015) 1302–1306.
[42] W.-D. Oh, Z. Dong, Z.-T. Hu, T.-T. Lim, J. Mater. Chem. A 3 (2015) 22208–22217.
[43] J. Michałowicz, Environ. Toxicol. Pharmacol. 37 (2014) 738–758.
[44] W. Sun, C. Wang, W. Pan, S. Li, B. Chen, Environ. Sci.: Nano 4 (2017) 1377–1388.
[45] T. Zhang, Y. Chen, Y. Wang, J. Le Roux, Y. Yang, J.-P. Croué, Environ. Sci. Technol. 48 (2014) 5868–5875.
[46] W.-D. Oh, S.-K. Lua, Z. Dong, T.-T. Lim, J. Mater. Chem. A 2 (2014) 15836–15845.
[47] Z.-T. Hu, J. Liu, X. Yan, W.-D. Oh, T.-T. Lim, Chem. Eng. J. 262 (2015) 1022–1032.
[48] Y. Wang, F. Li, T. Xue, C. Liu, D. Yuan, F. Qi, B. Xu, Environ. Sci. Pollut. Res. 25 (5) (2017) 4419–4434.
[49] H. Sun, X. Peng, S. Zhang, S. Liu, Y. Xiong, S. Tian, J. Fang, Bioresour. Technol. 241 (2017) 244–251.
[50] I. Saito, T. Matsuura, K. Inoue, J. Am. Chem. Soc. 103 (1981) 188–190.
[51] A. Tavakoli, A.A. Babaluo, K. Safaee, Fuller. Nanotube Carbon Nanostruct. 25 (2017) 312–317.
[52] H. Sun, C. Kwan, A. Suvorova, H.M. Ang, M.O. Tadé, S. Wang, Appl. Catal. B: Environ. 154–155 (2014) 134–141.
[53] C. Wang, J. Kang, H. Sun, H.M. Ang, M.O. Tadé, S. Wang, Carbon 102 (2016) 279–287.
[54] L. Lai, J.R. Potts, D. Zhan, L. Wang, C.K. Poh, C. Tang, H. Gong, Z. Shen, J. Lin, R.S. Ruoff, Energy Environ. Sci. 5 (2012) 7936–7942.
[55] D. Geng, Y. Chen, Y. Chen, Y. Li, R. Li, X. Sun, S. Ye, S. Knights, Energy Environ. Sci. 4 (2011) 760–764.